Synthetic Aperture Imaging of Multiple Point Targets in Rician Fading Media

Albert C. Fannjiang,* Knut Solna,† and Pengchong Yan‡

This paper presents an analysis of stability and detection for broad-band synthetic aperture imaging in Rician fading media. A main result is the stability condition $BNK^2/(K+1) \gg M$ where K is the Rician factor, B is the effective number of coherence bands, N is the effective number of array elements and M is the number of (widely separated) targets. A statistical scheme is introduced to reduce the uncertainty when the stability regime is not realized. The imaging methods are tested numerically with randomly distributed discrete scatterers and comparisons with the imaging with the full response matrices are made. The resolution study reveals several interesting effects: First, given the same measurement resources the synthetic aperture imaging has a better resolution performance, although is less stable, than the full response matrix imaging; second, for both imaging methods, the cross-range resolution decreases with the aperture (N fixed) and the antenna spacing (the total aperture fixed) while the range resolution increases with both parameters.

I. INTRODUCTION

We investigate synthetic aperture imaging in a cluttered environment with one antenna in this paper. An important feature of the propagation channel considered here is that the mean or coherent signals do not vanish. This is the case for what is called, in the wireless literature, *Rician fading channel* where in addition to incoherent signals there is a significant, nonfluctuating multipath component [15]. Typically a Rician channel arises when there is line-of-sight between the antennas and the targets.

The measurement configuration that we consider is motivated by Synthetic Aperture (SA) radars or lidars. SA imaging is a technique where a synthetic aperture is created by moving a source along a trajectory and repeatedly interrogating a search area by firing repeated pulses from the antenna and measuring the responses, see Fig. 1. This approach has many applications in remote sensing and elsewhere. The image formation is obtained via a matched filter technique and typically analyzed in the Born approximation [1]. This important imaging technique is however sensitive to noise and recent studies focus on the

*Electronic address: fannjiang@math.ucdavis.edu; The research supported in part by DARPA Grant N00014-02-1-0603.

†Electronic address: ksolna@math.uci.edu; The research supported in part by DARPA Grant N00014-02-1-0603 and partly also by NSF grant DMS0307011 and the Sloan Foundation

‡Electronic address: pyan@math.ucdavis.edu

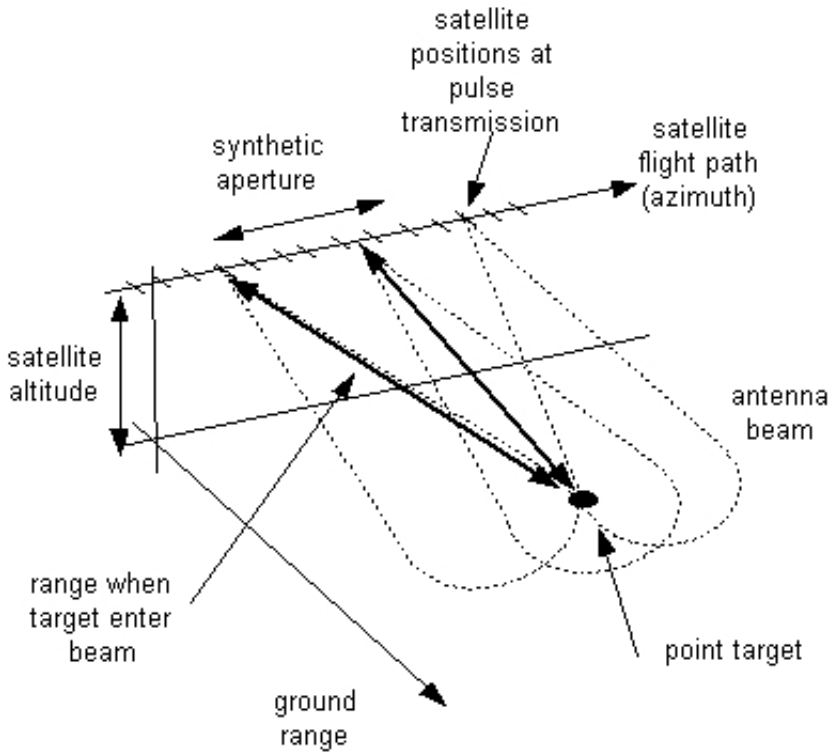

FIG. 1: Synthetic aperture radar (SAR) imaging configuration

role of noise in the image formation [18]. In synthetic aperture imaging high resolution is obtained via a chirped pulse combined with a deramping step.

In the present work we consider a simplified configuration with sampling at a set of well separated frequencies and a set of *fixed* probing locations along the measurement path, therefore neglecting the Doppler effect associated with the relative motion between the antenna and targets. In addition to simplify the stability and resolution analysis, this "static configuration" is also suitable in applications where the medium is time independent and the relative motion is slow. Our first main interest is then in the stability of the image formed from these measurements, that is, to what extent the image and the appearance of targets in it will depend sensitively on the particular clutter that happens to be in the scenery. This is a continuation of the work in [8].

Let M be the number of sufficiently separated (point) targets and B the number of sufficiently separated frequencies. Let K be the Rician factor which is the ratio of the coherent power to the fluctuating (incoherent) power. N be the number of sufficiently separated (point) antennas, Let N be the number of sufficiently separated measurement positions that the antenna will take in the whole process. Our study is not restricted to antenna paths of any particular geometry; they can be straight, circular or arbitrary.

We show that for a Rician fading channel a sufficient condition for imaging stability is

$$\frac{K^2}{K+1}BN \gg M. \tag{1}$$

In contrast, let us consider the following imaging configuration with a real, non-synthetic aperture: there is exactly one transmitting/receiving antenna at each of the N measurement positions. Each time an antenna emits a probing impulse all N antennas receive the responses. For each frequency, the impulse responses form a matrix called the response matrix or the multistatic data matrix. In comparison, SA imaging, as simplified here, uses only the diagonal elements of the response matrices. The imaging performance with the full response matrices has been analyzed previously [8] and shown to be stable if

$$KBN \gg M. \tag{2}$$

Condition (1) reduces to (2) when $K \gg 1$ i.e. the medium is nearly deterministic. On the other hand, when $K \ll 1$, (1) becomes $K^2BN \gg M$ which is significantly worse than (2). In the middle range $K \approx 1$, (1) is worse than (2) by a factor of two. The difference in the stability performance between the SA and the full response matrix imaging will be apparent in our numerical simulations (Figure 5).

The mean-zero case ($K = 0$) of the Rayleigh fading channels occurs in the diffuse regime which is beyond the scope of the present work. However it is noteworthy that the above stability condition bears certain resemblance to the stability condition for time reversal *communications* through the Rayleigh fading channels analyzed in [4] and [5].

In addition, our resolution analysis and numerical study reveal several interesting effects: (i) with N, B fixed the SA imaging, although less stable, has a better resolution performance than imaging with the response matrices; (ii) for both imaging methods, the cross-range resolution decreases with the aperture (with N fixed) and the antenna spacing (with the total aperture fixed) while the range resolution increases with both parameters.

Finally we develop a detection scheme to improve the imaging performance when the stability regime is not reached. We continue here the line of research set forth in [6].

II. MULTI-FREQUENCY ARRAY IMAGING

Let $H(\mathbf{x}, \mathbf{y}; \omega)$ be the transfer (a.k.a. Green) function of the propagation channel at the frequency ω from point $\mathbf{y}$ to $\mathbf{x}$. Denote $H_{mn}(\omega) = H(\mathbf{x}_m, \mathbf{y}_n; \omega)$. Let $\mathbf{H}(\omega) = [H_{mn}(\omega)]$ be the transfer matrix between the antennas located at $\mathbf{y}_n, 1 \le n \le N$ and targets located at $\mathbf{x}_m, 1 \le m \le M$. Reciprocity implies that $\mathbf{H}(\omega)$ is a symmetric matrix. Moreover, $H^*_{mn}(\omega) = H_{mn}(-\omega)$ where $*$ stands for complex conjugation.

We decompose the random transfer function into the mean $\bar{H}$ and the fluctuations $h, \mathbb{E}h = 0$, as

$$H(\mathbf{x}, \mathbf{y}; \omega) = \bar{H}(\mathbf{x}, \mathbf{y}; \omega) + h(\mathbf{x}, \mathbf{y}; \omega). \tag{3}$$

The mean and fluctuations are also known as the coherent and diffuse fields, respectively. We write $\bar{\mathbf{H}}(\omega) = [\bar{H}_{mn}(\omega)]$ and $\mathbf{h}(\omega) = [h_{mn}(\omega)]$ with $h_{mn}(\omega) = h(\mathbf{x}_m, \mathbf{y}_n; \omega)$.

Our main assumptions are (i) the separations of the frequencies $\omega_l, l = 1, 2, ..., B$ used for imaging are larger than the coherence bandwidth β_c of the channel (ii) the spacings of the antennas are wider than the coherence length ℓ_c of the channel, see here Section V B and [7] for a more detailed discussion. Moreover, we assume the idealized situation when h is circularly Gaussian with zero mean. As a result of these assumptions we have

$$\mathbb{E}\Big\{h_{ij}(\omega_k)h^*_{mn}(\omega_l)\Big\} \approx \eta^2\delta_{im}\delta_{jn}\delta_{k,l}, \quad \mathbb{E}\Big\{h_{ij}(\omega_k)h_{mn}(\omega_l)\Big\} \approx 0, \quad \forall i, j, m, n, \tag{4}$$

where η^2 is the intensity of fluctuations.

Let μ be the typical magnitude of the mean transfer function and let K be the Rician factor defined as

$$K = \frac{\mu^2}{\eta^2},$$

which will play an important role in the sequel. Let $u(\mathbf{x})$ be the imaging field (to be specified later) which is supposed to exhibit the location and the resolution of the hidden targets. We would like to derive the conditions under which the normalized variance of the imaging field u:

$$\mathfrak{R}(\mathbf{x}) = \frac{|\mathbb{E}u(\mathbf{x})|^2}{\mathbb{E}\big(|u|^2(\mathbf{x})\big) - |\mathbb{E}\big(u(\mathbf{x})\big)|^2},$$

tends to infinity. This is the stability result alluded to earlier. Note that $\mathfrak{R}(\mathbf{x})$ can be interpreted as a signal-to-interference ratio (SIR).

We assume that the multiple targets are point scatterers themselves but the multiple scattering effect involving the targets are negligible (e.g., when they are far apart and/or their scattering strength is weak). This assumption is a form of so called *distorted wave Born approximation* (DWBA). In the simulation presented in Section V A, the scattering strength of the targets is much smaller than that of the clutter so that DWBA is valid but the numerical scheme is exact and does not use DWBA.

We consider the method of the *differential response*. In this approach, probing signals of various frequencies are first used to survey the random media in the absence of targets. Then in the presence of targets (with unknown locations) the same set of probing signals are used again to survey the media which is assumed to be fixed. The differences between these two responses is called the differential responses which is then used to image the targets.

The differential responses received by the antenna at the location $\mathbf{y}_n$ for targets at locations $\mathbf{x}_i, 1 \le i \le M$ are, under the assumption of DWBA, given by $\sum_{i=1}^M \tau_i(\omega_l)H_{in}(\omega_l)H_{in}(\omega_l), l = 1, ..., B$. We then construct the imaging function by the matched-filter-type expression

$$u(\mathbf{x}) = \sum_{l=1}^{B}\sum_{i=1}^{M}\sum_{j=1}^{N} \tau_i(\omega_l)P(\mathbf{x}, \mathbf{y}_j; \omega_l)H^2_{ij}(\omega_l)P(\mathbf{y}_j, \mathbf{x}; \omega_l), \tag{5}$$

with $\tau_i(\omega_l)$ the reflectivity of target i at frequency ω_l. Following the analysis of [8] we use the *conjugate* phase-factor of the *mean* Green function as the back-propagator $P(\mathbf{x}, \mathbf{y}; \omega)$.

In practice, as discussed in Section IV, the *real* part of u tends to behave more stably than u itself and will be used as imaging function throughout the paper, even though for the sake of notational simplicity the stability analysis below is carried out for u.

III. STABILITY ANALYSIS

In this section we derive for Rician channels the stability condition (1). Under this stability condition the imaging field $u(\mathbf{x})$ is approximately equal to its mean $\mathbb{E}u(\mathbf{x})$.

Observe first that the expectation for u is given by

$$\begin{aligned}
\mathbb{E}u(\mathbf{x}) &= \sum_{l=1}^{B}\sum_{i=1}^{M}\sum_{n=1}^{N} \tau_i(\omega_l) P(\mathbf{x}, \mathbf{y}_n; \omega_l) \Big(\bar{H}_{in}^2(\omega_l) + \mathbb{E}\big[h_{in}^2(\omega_l)\big] \Big) P(\mathbf{y}_n, \mathbf{x}; \omega_l) \\
&\approx \sum_{l=1}^{B}\sum_{i=1}^{M}\sum_{n=1}^{N} \tau_i(\omega_l) P(\mathbf{x}, \mathbf{y}_n; \omega_l) \bar{H}_{in}^2(\omega_l) P(\mathbf{y}_n, \mathbf{x}; \omega_l) \\
&= O(|\tau| \mu^2 BN). \qquad (6)
\end{aligned}$$

Note that the apparent missing of a factor M in the above estimate is due to the choice of P as the phase-factor of the mean Green function. With this choice the leading contribution is from the few targets closest to the point $\mathbf{x}$ and thus there will be effectively only $O(1)$ terms in the above summation over i [8].

Note also that the expression for u contains a *product* of elements of $\mathbf{H}$. As a result, the expectation of u involves the second order moments of h and the variance of u involves the fourth order moments of h. In calculation of the fourth order moments we shall use the assumption of a Gaussian statistics. The Gaussian assumption is widely used and includes the Rician and Rayleigh fading channels in wireless modeling [3], [15].

Using the Gaussian moment assumption we obtain

$$\begin{aligned}
\mathbb{E}|u(\mathbf{x})|^2 \approx & \Big| \sum_{l=1}^{B}\sum_{i=1}^{M}\sum_{n=1}^{N} \tau_i(\omega_l) P(\mathbf{x}, \mathbf{y}_n; \omega_l) \bar{H}_{in}^2(\omega_l) P(\mathbf{y}_n, \mathbf{x}; \omega_l) \Big|^2 \\
& + 4\mathbb{E}\Big\{ \Big| \sum_{l=1}^{B}\sum_{i=1}^{M}\sum_{n=1}^{N} \tau_i(\omega_l) P(\mathbf{x}, \mathbf{y}_n; \omega_l) \bar{H}_{in} h_{in}(\omega_l) P(\mathbf{y}_n, \mathbf{x}; \omega_l) \Big|^2 \Big\} \\
& + \mathbb{E}\Big\{ \Big| \sum_{l=1}^{B}\sum_{i=1}^{M}\sum_{n=1}^{N} \tau_i(\omega_l) P(\mathbf{x}, \mathbf{y}_n; \omega_l) h_{in}^2(\omega_l) P(\mathbf{y}_n, \mathbf{x}; \omega_l) \Big|^2 \Big\} \qquad (7)
\end{aligned}$$

which becomes after using (4)

$$\mathbb{E}|u(\mathbf{x})|^2 \approx \big|\mathbb{E}u(\mathbf{x})\big|^2 + 2\eta^2 \sum_{l=1}^{B}\sum_{i=1}^{M}\sum_{n=1}^{N} |\tau_i(\omega_l)|^2 \big|P(\mathbf{x},\mathbf{y}_n;\omega_l)\big|^2 \bar{H}_{in} P(\mathbf{y}_n,\mathbf{x};\omega_l)\bar{H}^*_{in} P^*(\mathbf{y}_n,\mathbf{x};\omega_l)$$
$$+2\eta^2 \sum_{l=1}^{B}\sum_{i=1}^{M}\sum_{n=1}^{N} |\tau_i(\omega_l)|^2 P(\mathbf{x},\mathbf{y}_n;\omega_l)\bar{H}_{in}(\omega_l) P(\mathbf{y}_n;\mathbf{x};\omega_l) P^*(\mathbf{x},\mathbf{y}_n;\omega_l)\bar{H}^*_{in}(\omega_l) P^*(\mathbf{y}_n,\mathbf{x};\omega_l)$$
$$+\eta^4 \sum_{l=1}^{B}\sum_{i=1}^{M} |\tau_i(\omega_l)|^2 \sum_{n=1}^{N} \Big(\big|P(\mathbf{x},\mathbf{y}_n;\omega_l)\big|^2 \big|P(\mathbf{y}_n,\mathbf{x};\omega_l)\big|^2$$
$$+P(\mathbf{x},\mathbf{y}_n;\omega_l)P^*(\mathbf{y}_n,\mathbf{x};\omega_l)P^*(\mathbf{x},\mathbf{y}_n;\omega_l)P(\mathbf{y}_n,\mathbf{x};\omega_l)\Big)$$
$$= \big|\mathbb{E}u(\mathbf{x})\big|^2 + O(|\tau|^2\eta^2(\mu^2+\eta^2)BMN), \quad \text{as } B,N\to\infty. \tag{8}$$

Therefore, for an active array, we have $\mathfrak{R} \gg 1$ when (1) holds.

If the stability criterion (1) is satisfied then the coherent part of the imaging function corresponding to a target that appears clearly and does not depend sensitively on the particular clutter realization corresponding to a particular h.

IV. STATISTICAL DETECTION

For detection, it is more convenient to work with a real-valued imaging field such as the real-part of (5)

$$u_R(\mathbf{x}) \;=\; \Re\Big\{ \sum_{l=1}^{B}\sum_{i=1}^{M}\sum_{j=1}^{N} \tau_i(\omega_l) P(\mathbf{x},\mathbf{y}_j;\omega_l) H^2_{ij}(\omega_l) P(\mathbf{y}_j,\mathbf{x};\omega_l)\Big\}. \tag{9}$$

Moreover, since the absolute values of u and u_R are close to each other at the target locations and hence the numerical plot of $|u_R|$ often appears more stable than that of $|u|$, see Figure 4.

Under the Gaussian assumption expression (9) has a χ^2 distribution. To simplify the discussion we neglect the quadratic-in-h terms. This can be justified when, e.g. $K \gg 1$, see Appendix B. Then (9) becomes

$$u_R(\mathbf{x}) \;=\; \Re\Big\{ \sum_{l=1}^{B}\sum_{i=1}^{M}\sum_{j=1}^{N} \tau_i(\omega_l) P(\mathbf{x},\mathbf{y}_j;\omega_l)\big(\bar{H}^2_{ij}(\omega_l) + 2\bar{H}_{ij}(\omega_l)h_{ij}(\omega_l)\big) P(\mathbf{y}_j,\mathbf{x};\omega_l)\Big\} \tag{10}$$

which has the Gaussian distribution of the mean and variance:

$$\mathbb{E}(u_R(\mathbf{x})) = \Re\Big\{\sum_{l=1}^{B}\sum_{i=1}^{M}\sum_{j=1}^{N}\tau_i(\omega_l)P(\mathbf{x},\mathbf{y}_j;\omega_l)\bar{H}_{ij}^2(\omega_l)P(\mathbf{y}_j,\mathbf{x};\omega_l)\Big\} \tag{11}$$

$$\begin{aligned}\mathrm{Var}(u_R(\mathbf{x})) &= 2\eta^2\sum_{l=1}^{B}\sum_{i=1}^{M}\sum_{j=1}^{N}|\tau_i(\omega_l)|^2|P(\mathbf{x},\mathbf{y}_j;\omega_l)|^2|P(\mathbf{y}_j,\mathbf{x};\omega_l)|^2|\bar{H}_{ij}(\omega_l)|^2\\ &= 2\eta^2\sum_{l=1}^{B}\sum_{i=1}^{M}\sum_{j=1}^{N}|\tau_i(\omega_l)|^2|\bar{H}_{ij}(\omega_l)|^2. \end{aligned}\tag{12}$$

Here we have used the fact $|P(\mathbf{x},\mathbf{y};\omega)| = 1$ since the back-propagator P is chosen to be the *conjugate* phase factor of the mean Green function. For simplicity we consider the case of identical point targets $\tau_i = \tau, i = 1, ..., M$.

For each point $\mathbf{x}$ in the search domain, we postulate the alternatives:

$$\begin{cases}\mathcal{H}_0(\mathbf{x}): & \mathbf{x} \text{ is far away from any target;}\\ \mathcal{H}_1(\mathbf{x}): & \mathbf{x} \text{ is close to a target.}\end{cases}$$

By the assumption that the targets are widely separated, the mean of u_R under hypothesis $\mathcal{H}_0$ should be approximately zero while under $\mathcal{H}_1$ it can be approximated by

$$\nu(\mathbf{x}) = \sum_{l=1}^{B}\sum_{j=1}^{N}\tau(\omega_l)|\bar{H}(\mathbf{x},\mathbf{y}_j;\omega_l)|^2, \tag{13}$$

in view of (11), since one target will dominate the summation over i in (11). (13) can be calculated with the knowledge of τ and $\bar{H}$. On the other hand, the variance under either hypothesis is the same as

$$\sigma^2 = 2\eta^2\sum_{l=1}^{B}\sum_{i=1}^{M}\sum_{j=1}^{N}|\tau(\omega_l)|^2|\bar{H}_{ij}(\omega_l)|^2$$

which is independent of the test point $\mathbf{x}$ but dependent on the locations of the targets.

In the numerical experiment below, we make the approximation $|\bar{H}_{ij}(\omega_l)| \approx \mu(\omega_l)$ assuming that the targets are roughly the same distance from the array and estimate σ^2 to be

$$\sigma^2 \approx 2\eta^2 MN\sum_{l}^{B}|\tau(\omega_l)|^2\mu(\omega_l) \tag{14}$$

assuming that the total number M of point targets is known.

The Neyman-Pearson lemma states that when choosing between $\mathcal{H}_0$ and $\mathcal{H}_1$ with a prescribed false alarm rate α the likelihood ratio test that rejects $\mathcal{H}_0$ in favor of $\mathcal{H}_1$ if the

corresponding likelihood is above a threshold (e^γ) is the most powerful test. The threshold is determined by

$$\frac{\text{p.d.f. of } u_R(\mathbf{x})|_{\mathcal{H}_1}}{\text{p.d.f. of } u_R(\mathbf{x})|_{\mathcal{H}_0}} = e^{-\frac{1}{2\sigma^2}(u_R-\nu)^2} / e^{-\frac{1}{2\sigma^2}u_R^2} = e^{-\frac{1}{2\sigma^2}(-2u_R\nu+\nu^2)} > e^\gamma \tag{15}$$

which implies

$$\frac{u_R}{\sigma} > \frac{\gamma\sigma}{\nu} + \frac{\nu}{2\sigma}. \tag{16}$$

Under the hypothesis $\mathcal{H}_0$,

$$Y_0 \equiv \frac{u_R}{\sigma} \sim N(0,1).$$

Consequently, for the false alarm rate α we have

$$\frac{\gamma\sigma}{\nu} + \frac{\nu}{2\sigma} = Q^{-1}(1-\alpha),$$

where Q is the standard *cumulative* Gaussian probability function. Hence

$$\gamma = \frac{\nu}{\sigma}Q^{-1}(1-\alpha) - \frac{\nu^2}{2\sigma^2} \tag{17}$$

On the other hand, under the hypothesis $\mathcal{H}_1$,

$$Y_1 \equiv \frac{u_R - \nu}{\sigma} \sim N(0,1)$$

and the detection rule (16) gives rise to a miss probability β satisfying

$$\frac{\gamma\sigma}{\nu} - \frac{\nu}{2\sigma} = Q^{-1}(\beta). \tag{18}$$

By (17) and (18), we obtain the detection rate $P_d \equiv 1-\beta$ as a function of α:

$$P_d = 1 - Q(Q^{-1}(1-\alpha) - \frac{\nu}{\sigma}). \tag{19}$$

The graphs of P_d as a function of α are called the Receiver Operating Characteristic (ROC) curves which are parametrized by the unknown $\nu(\mathbf{x})/\sigma$.

The ROC curves are shown in Fig. 2 with $B = 20$, $N = 6$, $M = 7$ and different K's. For these parameters, the quadratic-in-h terms in the imaging function begin to have a smaller magnitude than the linear-in-h terms for $K > 1/2$. Although the curves are determined by ν/σ only, they are different at any search point $\mathbf{x}$ because the Rician factor K is a function of the location $\mathbf{x}$ in general.

Clearly the above detection scheme is based on some rough approximations and not entirely satisfactory. Moreover, the extension to the case with significantly varying τ's and distances from the aperture is cumbersome. In our numerical experiments, however, it seems to have a reasonable performance with a suitably chosen false alarm rate (Figure 8).

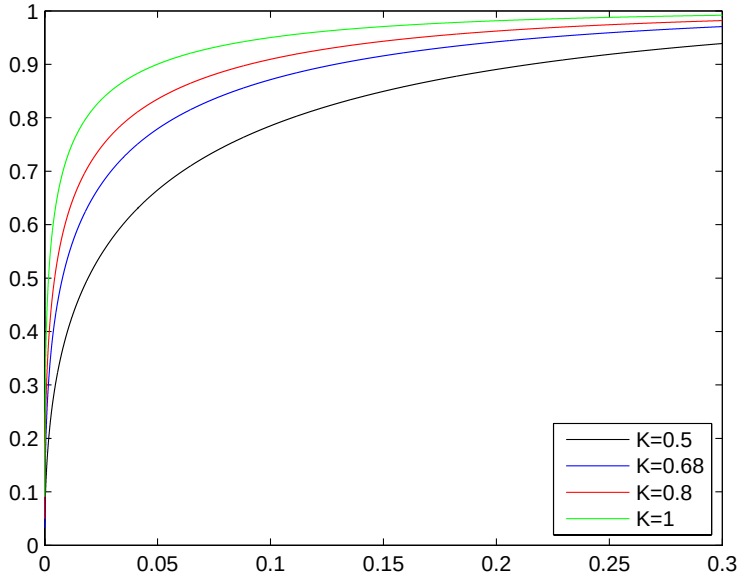

FIG. 2: ROC curves with $B = 20$ frequencies, $N = 6$ antennas, and $M = 7$ targets at various K's.

V. RANDOMLY DISTRIBUTED POINT SCATTERERS

In this section we present first the Foldy-Lax formulation which defines the point scatterer model that we use for the simulations, see [9, 13, 14]. This model also gives directly a numerical scheme for computing the channel response and we comment on this scheme in more detail in Appendix A. An important ingredient in the matched field imaging is the choice for propagator that give the imaging function via backpropagation. The matched field corresponds to applying the adjoint of the mapping from scattering medium to observations. It can be interpreted respectively as backpropagation or time reversal of the observed field. We comment in Section V B on the mean (Green's) field that follows from effective medium theory and how it relates to the imaging function. Then we present some numerical results for our imaging scheme using only the raw imaging function $u_R(\mathbf{x})$ as well as the detection based scheme that we introduced above.

A. Foldy-Lax formulation

We discuss the discrete model with many point scatterers randomly distributed throughout the space. We refer the reader to the next section for discussion of the mean Green's function, especially its phase factor, of this case, see (22) in particular.

Let the randomly distributed point scatterers of refractive index n_j be located at $\mathbf{r}_j, j =$

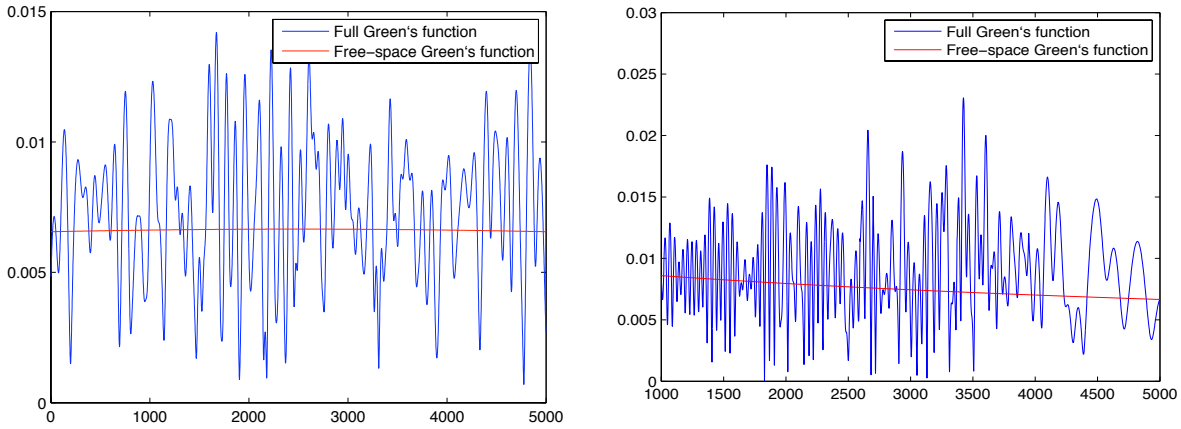

FIG. 3: The transverse (left), at $x = 5000$, and longitudinal (right), at $y = 2500$, profiles of the intensity of the Green function at wavelength 70 with 1000 randomly distributed particles whose $n^2 - 1$ is 70.

$1, 2, 3, ...J$ and let $G(\mathbf{x}, \mathbf{y}; \omega_l)$ be the Green's function. Then the Lippman-Schwinger equation becomes in this case [12]

$$G(\mathbf{x}, \mathbf{y}_n; \omega_l) = G_0(\mathbf{x}, \mathbf{y}_n; \omega_l) + \sum_{j=1}^{J} \tau_j(\omega_l) G_0(\mathbf{x}, \mathbf{r}_j; \omega_l) G(\mathbf{r}_j, \mathbf{y}_n; \omega_l), \quad n = 1, ..., N$$

where the scattering strength τ_j of the j-th scatterer is given by

$$\tau_j(\omega_l) = \omega_l^2 (n_j^2 - 1). \tag{20}$$

The Lippman-Schwinger equation is valid for all $\mathbf{x}$ except at the actual scatterer locations $\mathbf{x} = \mathbf{r}_i$. Thus, to determine $G(\mathbf{r}_j, \mathbf{y}_n; \omega_l)$, we replace the Lippman-Schwinger equation by the Foldy-Lax equation

$$G(\mathbf{r}_m, \mathbf{y}_n; \omega_l) = G_0(\mathbf{r}_m, \mathbf{y}_n; \omega_l) + \sum_{j=1 \neq m}^{J} \tau_j(\omega_l) G_0(\mathbf{r}_m, \mathbf{r}_j; \omega_l) G(\mathbf{r}_j, \mathbf{y}_n; \omega_l), \quad n = 1, ..., N \tag{21}$$

where the divergent self-field term has been removed. Finding the field $G(\mathbf{r}_j, \mathbf{y}_n; \omega_l)$ is then reduced to inverting a matrix with entries

$$\delta_{ij} - (1 - \delta_{ij}) \tau_j G_0(\mathbf{r}_i, \mathbf{r}_j), \quad i, j = 1, 2, ...J.$$

Once the $G(\mathbf{r}_j, \mathbf{y}_n; \omega_l)$s are determined, they can be substituted in the Lippman-Schwinger equation to find the wave field at any location. The numerical scheme is further explicated in Appendix A.

In our simulations, 1000 or 3000 point scatterers are uniformly randomly distributed in the domain $[2000, 4000] \times [0, 5000]$, while the whole computation domain is $[-5000, 5000] \times [0, 5000]$. Some profiles of the Green function are shown in Fig. 3

B. Phase factor of the mean Green function

According to the effective medium theory, the mean transfer function in three spatial dimensions takes the following form

$$\bar{H}(\mathbf{x},\mathbf{y};\omega) \sim e^{-\frac{r}{2\ell}}\frac{e^{ikr}}{r}, \quad r = |\mathbf{x}-\mathbf{y}|, \tag{22}$$

where the mean-free path ℓ is related to the extinction cross section σ_t by

$$\ell = \frac{1}{\rho\sigma_t},$$

with ρ density of particles. Note that when the particle size a is much greater than the wavelength λ, $\sigma_t \approx 2\pi a^2$, $a =$ radius of particles, and independent of frequency.

On the other hand, when the particle size is much smaller than the wavelength, the extinction cross section usually depends on the frequency as well. In the case of Rayleigh scattering without absorption, the scattering cross section scales like ω^{-4}

$$\ell \sim \rho^{-1}(c_0/\omega)^4 a^{-6} \tag{23}$$

where c_0 is the background phase velocity [12] In the formulation of the matched field we retain only the travel time part of the mean Green's function, corresponding to: e^{ikr}, and back-propagation of the wave field.

C. Imaging and detection simulations

In the simulations we use $N = 6$ or 11 antennas equally spaced on the side $x = -5000, y \in [1500, 3500]$ (total aperture $A = 2000$) and $B = 20$ frequencies corresponding to *equally spaced wavelengths* in the range from 52 to 90. Recall also that the imaging is based on the difference field. Seven targets are located at $[3100, 100]$, $[2800, 1000]$, $[4000, 1600]$, $[3300, 2100]$, $[4500, 3000]$, $[3000, 4000]$, and $[3500, 4800]$. As explained in Appendix A, we do not make use of distorted wave Born approximation.

Figure 4 demonstrates that u_R is a more stable imaging function than u itself and that the imaging performance deteriorates as the number of clutter particles increases.

Figure 5 shows the difference in the stability performance between the imaging with SA and the response matrices (i.e. for each source location the reflected field is measured at all other antenna positions). The SA imaging configuration corresponds to having available only the diagonal elements of the response matrices and hence is generally less stable as our stability analysis predicts.

Figure 6 and Figure 7 show the numerical resolution curves for one target point in the medium with 1000 scatterers and the free-space, respectively. The resolution (vertical axis) is defined as the distance from the target where the the imaging function has dropped to

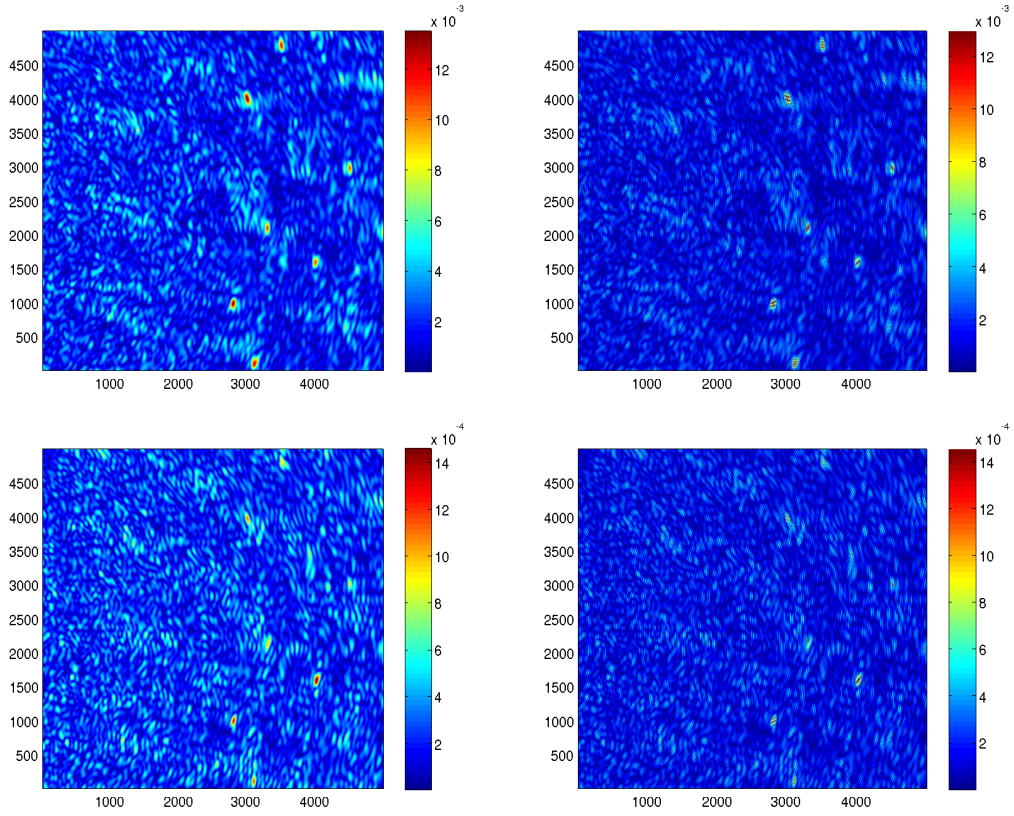

FIG. 4: $|u|$ (left) v.s. $|u_R|$ (right) for seven targets with 20 frequencies and 11 antennas (total aperture = 2000). $n^2 - 1$ of the clutter and the targets are 50 and 1, respetively. The top plots are simulated with 1000 particles and the bottom plots with 3000 particles. Note the difference in magnitude between the top and the bottom plots. The plots of $|u_R|$ tend to be more stable than those of $|u|$.

half of its value at the target location. And for each case we compare the SA resolution to that with the full response matrices .

Three interesting observations are in order.

(i) The SA resolution is consistently better than that with the full response matrices. The difference is more pronounced in the cross-range resolution than in the range resolution.

(ii) The cross-range resolutions in both cases decrease with the aperture, consistent with the physical intuition. On the contrary, the range resolutions in both cases increase (slowly) with the aperture. In this comparative study, the number of antennas $N = 11$ is fixed.

(iii) Also, not shown in the figures, the resolutions have a similar behavior with respect to the change in the antenna spacing (with A fixed, hence N changing accordingly).

In Appendices B and C we give an asymptotic analysis supporting these counterintuitive

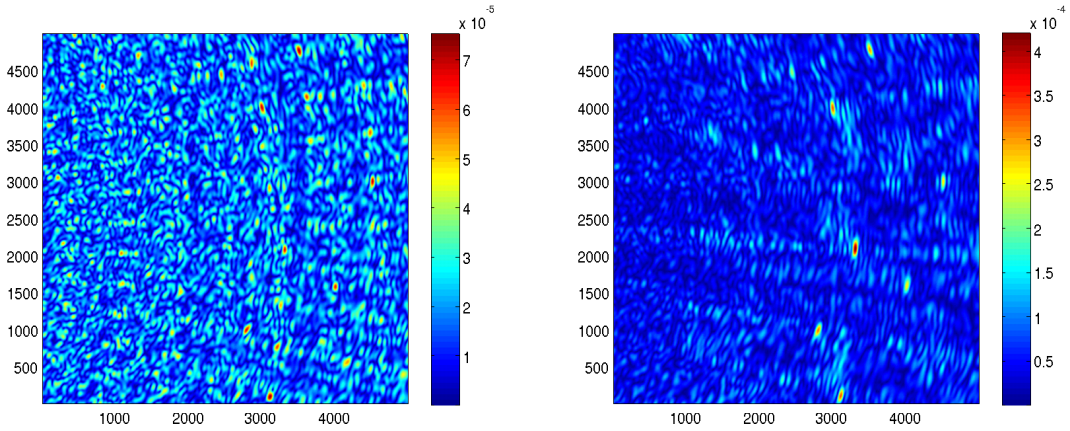

FIG. 5: SA (left) and full response matrix (right) imaging plots of $|u|$ with seven targets cluttered by 1000 particles and 6 antennas (total aperture = 2000). $n^2 - 1$ of the clutter and the targets is 70 and 1, respectively. Note the difference in the magnitude scale between the two plots. The plot on the left is less stable than the plot on the right, as the theory predicts. The SA imaging plot here is also less stable than the plots on the left column in Figure 4 due to the increase in the clutter reflectivity and the decrease in the antenna number. In Figure 8, where $|u_R|$, instead of $|u|$ is plotted, the SA imaging is improved by using a statistical detection scheme.

effects.

Finally we apply the statistical detection scheme to reduce the level of uncertainty. The result is shown in Figure 8 (right). Note that the image now is "cleaned-up" relative to the raw image.

VI. CONCLUSIONS

We have revisited the problem of imaging a set of point targets based on the scattered wave field at a number of discrete frequencies as recorded by an antenna array. The target scatterers are masked by a large number of "clutter" particles. Here we consider a SA imaging array and use difference field for imaging. When imaging in clutter it is fundamental to identify whether the constructed image will be statistically stable, meaning that the coherent features in the image that corresponds to the target scatterers dominate the incoherent noise caused by the clutter. We have identified a fundamental sampling criterion that must be satisfied for having statistical stability that essentially says that the Rician number of the channel must be large relative to the ratio of the target degrees of freedom to the measurement degree of freedom. We have also set forth a hypothesis based framework that gives an explicit rule for deciding on the presence of a scatterer at a particular location, which optimally adapts to the clutter present in the scenery at hand. Finally our resolution analysis

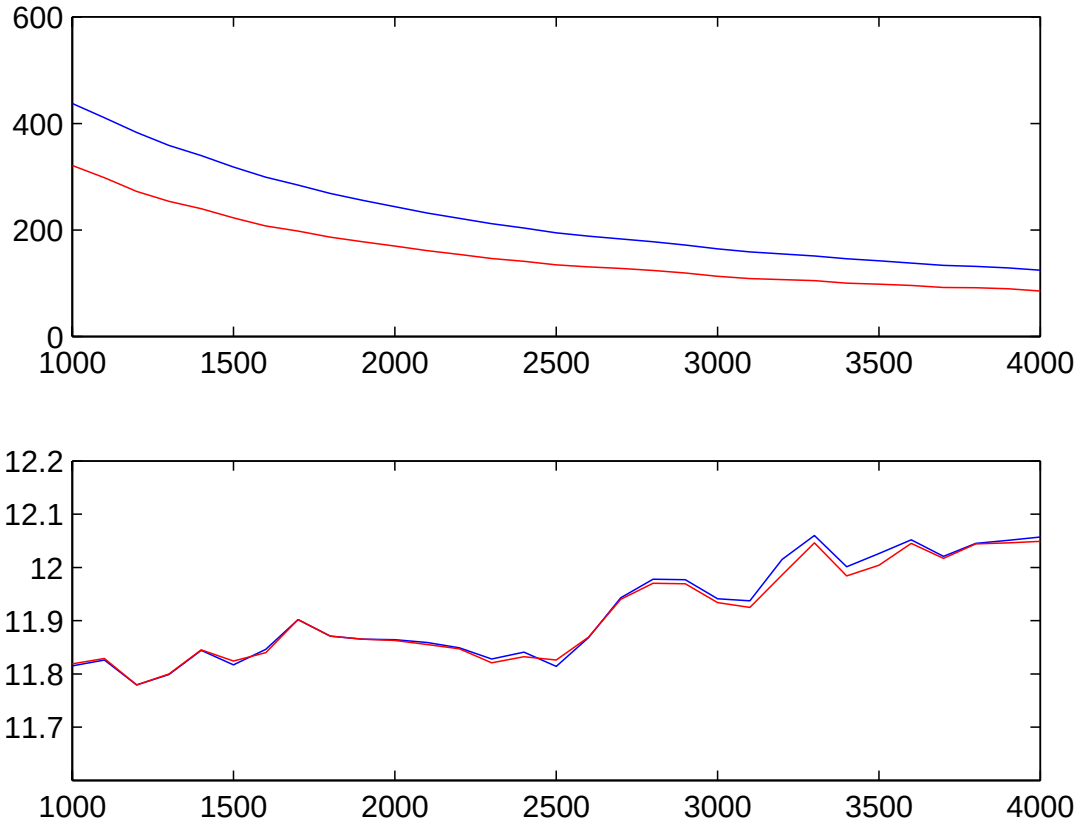

FIG. 6: Comparison of range (bottom) and cross-range (top) resolutions with synthetic aperture (red) and full response matrices (blue). $n^2 - 1$ of the clutter and the target equal to 50 and 1, respectively. 11 antennas and 1000 particles are used in the simulation. The horizontal axis is the aperture size.

have revealed several interesting effects: First, given the same measurement resources (N, B) SA imaging has a better resolution performance, although is less stable, than response matrix imaging; second, for both imaging methods, the cross-range resolution decreases with the aperture and the antenna spacing while the range resolution increases (slightly) with the two parameters.

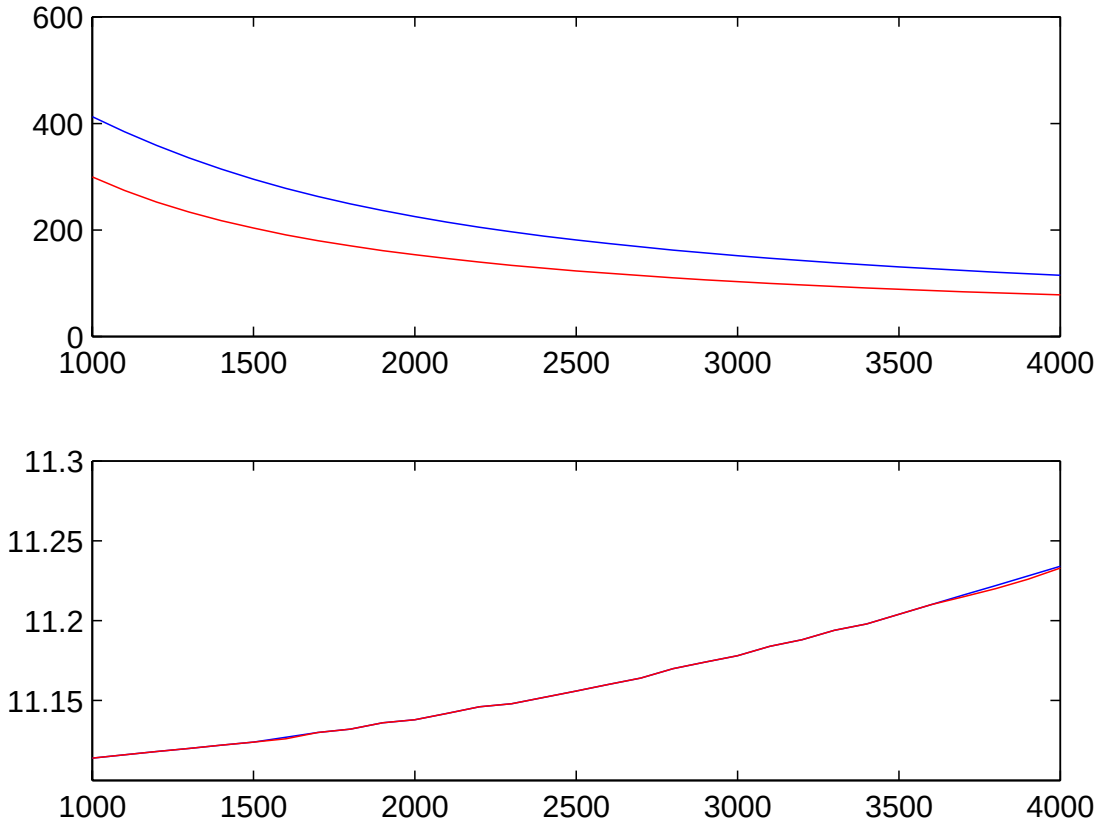

FIG. 7: Resolutions for the free space: the range (bottom) and cross-range (top) resolutions with synthetic aperture (red) and full response matrices (blue).

Appendix A: The Foldy-Lax formulation

Let $\mathbf{x}_m, m = 1, ..., M$ be the locations of the M target points and $\mathbf{x}_{M+j}, j = 1, ..., J$ the locations of the J clutter points. The wave field $U(\mathbf{r}, \omega)$ for a source at $\mathbf{y}_i$ in the presence of both clutter and target particles satisfies

$$U(\mathbf{r}, \omega) = G_0(\mathbf{y}_i, \mathbf{r}; \omega) + \sum_{m=1}^{M+J} \tau(\mathbf{x}_m, \omega) G_0(\mathbf{r}, \mathbf{x}_m; \omega) U(\mathbf{x}_m, \omega) \tag{A1}$$

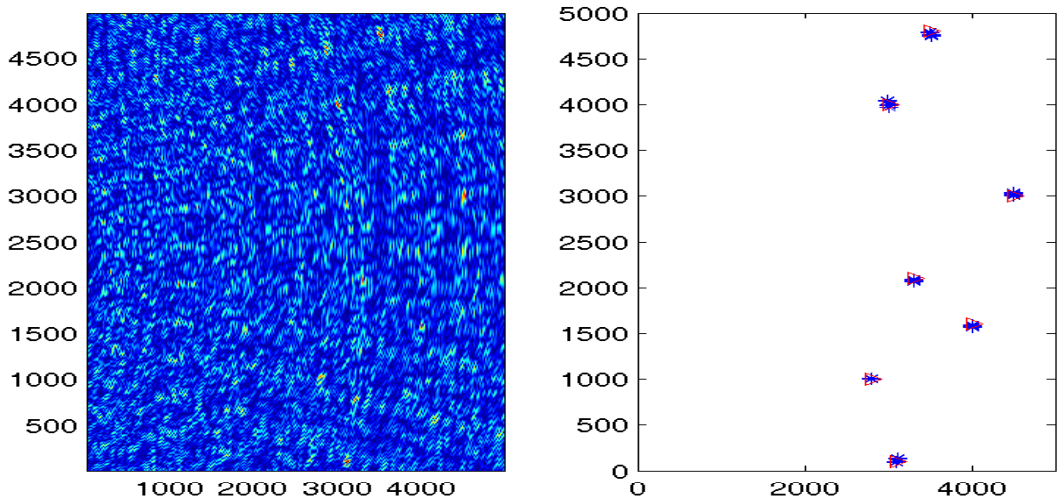

FIG. 8: SA imaging plot of $|u_R|$ (left) and statistical detection figure (right) of 7 targets with 6 transducers and 20 frequencies. The number of clutter scatterers is 1000. $n^2 - 1$ of the clutter and the targets are 70 and 1, respectively. The false-alarm-rate α of the detection algorithm is 0.15%. The red triangles denote the true targets' locations and the blue stars are the results of the detection. When α is low, it is possible to miss some of the targets and when α is high, false targets may show up.

The scattering amplitude function at scatterer m is $\tau_m = \tau(\mathbf{x}_m, \omega)$. Evaluation at the scatterers then gives the Foldy-Lax equations:

$$U(\mathbf{x}_j, \omega) \;=\; G_0(\mathbf{y}_i, \mathbf{x}_1; \omega) + \sum_{m \neq j} \tau_m G_0(\mathbf{x}_1, \mathbf{x}_m; \omega) U(\mathbf{x}_m, \omega), \quad j = 1, ..., M + J.$$

Consequently, the wave field at the target locations is determined by

$$\begin{pmatrix} U(\mathbf{x}_1, \omega) \\ U(\mathbf{x}_2, \omega) \\ \vdots \\ U(\mathbf{x}_{M+J}, \omega) \end{pmatrix} \;=\; \mathbf{F}_\omega^{-1} \begin{pmatrix} G_0(\mathbf{y}_i, \mathbf{x}_1; \omega) \\ G_0(\mathbf{y}_i, \mathbf{x}_2; \omega) \\ \vdots \\ G_0(\mathbf{y}_i, \mathbf{x}_{M+J}; \omega) \end{pmatrix} \tag{A2}$$

where

$$\mathbf{F}_\omega \;=\; \begin{pmatrix} 1 & -\tau_2 G_0(\mathbf{x}_1, \mathbf{x}_2; \omega) & \dots & -\tau_{M+J} G_0(\mathbf{x}_1, \mathbf{x}_{M+J}; \omega) \\ -\tau_1 G_0(\mathbf{x}_2, \mathbf{x}_1; \omega) & 1 & \dots & -\tau_{M+J} G_0(\mathbf{x}_2, \mathbf{x}_{M+J}; \omega) \\ \dots & \dots & \ddots & \dots \\ -\tau_1 G_0(\mathbf{x}_{M+J}, \mathbf{x}_1; \omega) & -\tau_2 G_0(\mathbf{x}_{M+J}, \mathbf{x}_2; \omega) & \dots & 1 \end{pmatrix}.$$

The vector on the left hand side of (A2) in turn determines the scattered field through (A1).

For $m = 1, \ldots, M + J$, define the vector $\vec{G}_0(\mathbf{x}_m)$ as

$$\vec{G}_0(\mathbf{x}_m, \omega) = (G_0(\mathbf{x}_m, \mathbf{y}_1; \omega), G_0(\mathbf{x}_m, \mathbf{y}_2; \omega), \ldots, G_0(\mathbf{x}_m, \mathbf{y}_N; \omega))^T.$$

The full response matrix R is an $N \times N$ square matrix given by

$$R(\omega) = \begin{pmatrix} \tau_1 \vec{G}_0(\mathbf{x}_1, \omega) & \tau_2 \vec{G}_0(\mathbf{x}_2, \omega) & \ldots & \tau_{M+J} \vec{G}_0(\mathbf{x}_{M+J}, \omega) \end{pmatrix} \mathbf{F}_\omega^{-1} \begin{pmatrix} \vec{G}_0^T(\mathbf{x}_1, \omega) \\ \vec{G}_0^T(\mathbf{x}_2, \omega) \\ \vdots \\ \vec{G}_0^T(\mathbf{x}_{M+J}, \omega) \end{pmatrix}$$

where T denotes the matrix transpose.

Similarly, we can simulate the wave fields in the presence of clutter particles only. Note that in the Foldy-Lax simulation, we do not make the DWBA assumption.

Appendix B: Reduced Imaging Field

We show that under the condition $K \gg 1$ the quadratic-in-h terms in (9) is negligible. First we write explicitly

$$\begin{aligned} u_R(\mathbf{x}) &= \Re\Big\{ \sum_{l=1}^{B} \sum_{i=1}^{M} \sum_{j=1}^{N} \tau_i(\omega_l) P(\mathbf{x}, \mathbf{y}_j; \omega_l) H_{ij}^2(\omega_l) P(\mathbf{y}_j, \mathbf{x}; \omega_l) \Big\} \\ &= \Re\Big\{ \sum_{l=1}^{B} \sum_{i=1}^{M} \sum_{j=1}^{N} \tau_i(\omega_l) P(\mathbf{x}, \mathbf{y}_j; \omega_l) \bar{H}_{ij}^2(\omega_l) P(\mathbf{y}_j, \mathbf{x}; \omega_l) \Big\} \qquad \text{(B1)} \\ &\quad + \Re\Big\{ \sum_{l=1}^{B} \sum_{i=1}^{M} \sum_{j=1}^{N} \tau_i(\omega_l) P(\mathbf{x}, \mathbf{y}_j; \omega_l) 2\bar{H}_{ij}(\omega_l) h_{ij}(\omega_l) P(\mathbf{y}_j, \mathbf{x}; \omega_l) \Big\} \qquad \text{(B2)} \\ &\quad + \Re\Big\{ \sum_{l=1}^{B} \sum_{i=1}^{M} \sum_{j=1}^{N} \tau_i(\omega_l) P(\mathbf{x}, \mathbf{y}_j; \omega_l) h_{ij}^2(\omega_l) P(\mathbf{y}_j, \mathbf{x}; \omega_l) \Big\} \qquad \text{(B3)} \end{aligned}$$

The (B1) term is a deterministic term, while the (B2) and (B3) terms are random with mean zero. We show next that the variance of (B2) is larger than that of (B3) in the case $K \gg 1$.

The variance of (B2) is

$$\begin{aligned} & 2\eta^2 \sum_{l=1}^{B} \sum_{i=1}^{M} \sum_{j=1}^{N} |\tau_i(\omega_l)|^2 |P(\mathbf{x}, \mathbf{y}_j; \omega_l)|^2 |P(\mathbf{y}_j, \mathbf{x}; \omega_l)|^2 |\bar{H}_{ij}(\omega_l)|^2 \\ = \; & 2\eta^2 \sum_{l=1}^{B} \sum_{i=1}^{M} \sum_{j=1}^{N} |\tau_i(\omega_l)|^2 |\bar{H}_{ij}(\omega_l)|^2 \\ \approx \; & 2\mu^2 \eta^2 BMN |\tau|^2, \end{aligned}$$

and the variance of (B3) is

$$\begin{aligned}
&\eta^4 \sum_{l=1}^{B}\sum_{i=1}^{M}\sum_{j=1}^{N} |\tau_i(\omega_l)|^2 |P(\mathbf{x},\mathbf{y}_j;\omega_l)|^2 |P(\mathbf{y}_j,\mathbf{x};\omega_l)|^2 \\
=\ &\eta^4 \sum_{l=1}^{B}\sum_{i=1}^{M}\sum_{j=1}^{N} |\tau_i(\omega_l)|^2 \\
\approx\ &\eta^4 BMN|\tau|^2.
\end{aligned}$$

The ratio of the former to the latter is proportional to $K \gg 1$.

Appendix C: Cross-range resolution

To simplify the resolution analysis we use the paraxial approximation and consider the two dimensional case. The Green function for the paraxial wave in the free space is

$$G_0(x,z) = e^{ikz}\sqrt{\frac{k}{i2\pi z}}\exp\left[i\frac{kx^2}{2z}\right] \tag{C1}$$

where z and x are the longitudinal and transverse coordinates, respectively. In the associated random counterpart called the Markovian model [17], the mean Green function has a similar form

$$\bar{G}(x,z) = e^{-k^2C_0z}e^{ikz}\sqrt{\frac{k}{i2\pi z}}\exp\left[i\frac{kx^2}{2z}\right] \tag{C2}$$

which again has the same phase factor as the free space Green function. Since we assume the stability regime, the Markovian model and the free-space case yield the similar results. So we will focus on the resolution analysis for one point target in the free space.

We choose the unit system so that the phase velocity is one and $\omega = k$.

1. Imaging with the response matrices

Let (x_0, z_0) be the location of the target. The imaging field u with the full response matrices is

$$u(x,z) \ =\ \frac{1}{2\pi}\sum_{l=1}^{B}\sum_{n,j=1}^{N} |\omega_l| z_0^{-1} e^{2i\omega_l(z_0-z)} e^{-i\frac{\omega_l|x-y_n|^2}{2z}} e^{i\frac{\omega_l|x_0-y_n|^2}{2z_0}} e^{-i\frac{\omega_l|x-y_j|^2}{2z}} e^{i\frac{\omega_l|x_0-y_j|^2}{2z_0}} \tag{C3}$$

For convenience we use an even number of frequencies such that $\omega_i = -\omega_{B+1-i}$ ($i = 1,\ldots,B/2$). Consequently, the imaging field (C3) is real-valued.

Set $z = z_0$ and use the approximation

$$\sum_{n=1}^{N} e^{-i\frac{\omega_l|x-y_n|^2}{2z_0}} e^{i\frac{\omega_l|x_0-y_n|^2}{2z_0}}$$
$$\approx \Big(e^{i\ell_a\omega_l(x-x_0)/z_0} - 1\Big)^{-1} e^{-i\frac{\omega_l}{2z_0}(x^2-|x_0|^2)}\Big(e^{-i\frac{\omega_l}{z_0}(x_0-x)\cdot y_{N+1}} - e^{-i\frac{\omega_l}{z_1}(x_0-x)\cdot y_1}\Big), \qquad \text{(C4)}$$

assuming that $|\ell_a\omega_l(x_0 - x)| \ll z_0$ where ℓ_a is the antenna spacing. Hence we have

$$\begin{aligned} u(x, z_0) \;&\approx\; \frac{1}{2\pi}\sum_{l=1}^{B}\sum_{n,j=1}^{N} |\omega_l| z_0^{-1} e^{-i\frac{\omega_l}{z_0}(|x|^2-|x_0|^2)} \\ &\times\; \Big(e^{i\ell_a\omega_l(x-x_0)/z_0} - 1\Big)^{-2}\Big(e^{i\frac{\omega_l}{z_0}(x-x_0)\cdot y_{N+1}} - e^{i\frac{\omega_l}{z_0}(x-x_0)\cdot y_1}\Big)^2 \end{aligned}$$

Suppose that $\epsilon \equiv x - x_0$ is so small that the expansion in the powers of ϵ can be truncated at the second order, namely

$$\begin{aligned} e^{-i\frac{\omega_l}{z_0}(x^2-|x_0|^2)} \;&=\; 1 - i\frac{\omega_l}{z_0}\epsilon(2x_0+\epsilon) - \frac{\omega_l^2}{2z_0^2}\epsilon^2(2x_0+\epsilon)^2 + o(\epsilon^2) \\ &=\; 1 - i\epsilon\frac{2\omega_l x_0}{z_0} - \epsilon^2(i\frac{\omega_l}{z_0} + \frac{2\omega_l^2 x_0^{\perp 2}}{z_0^2}) + o(\epsilon^2), \end{aligned}$$

$$\Big(e^{i\ell_a\omega_l(x-x_0)/z_0} - 1\Big)^{-2} \;=\; \frac{-z_0^2}{\omega_l^2\ell_a^2\epsilon^2}\Big(1 - \frac{i\omega_l\ell_a\epsilon}{z_0} - \frac{5\omega_l^2\ell_a^2\epsilon^2}{12z_0^2} + O(\epsilon^2)\Big)$$

and

$$\begin{aligned} e^{i\frac{\omega_l}{z_0}(x-x_0)\cdot y_{N+1}} - e^{i\frac{\omega_l}{z_0}(x-x_0)\cdot y_1} \;&=\; i\epsilon N\ell_a\frac{\omega_l}{z_0}\Big\{1 + \frac{i\omega_l}{2z_0}\epsilon(y_{N+1}+y_1) \\ &\quad -\frac{\omega_l^2}{6z_0^2}\epsilon^2(y_{N+1}^2 + y_{N+1}y_1 + y_1^2)\Big\} + o(\epsilon^2). \end{aligned}$$

Then the imaging function becomes

$$\begin{aligned} &u(z_0, x) \\ &= \frac{N^2}{2\pi z_0}\sum_{l=1}^{B}|\omega_l|\Big(1 - \frac{i\omega_l\ell_a\epsilon}{z_0} - \frac{5\omega_l^2\ell_a^2\epsilon^2}{12z_0^2}\Big)\Big(1 - i\epsilon\frac{2\omega_l x_0}{z_0} - \epsilon^2(i\frac{\omega_l}{z_0} + \frac{2\omega_l^2 x_0^{\perp 2}}{z_0^2})\Big) \\ &\times\Big(1 + \frac{i\omega_l}{2z_0}\epsilon(y_{N+1}+y_1) - \frac{\omega_l^2}{6z_0^2}\epsilon^2(y_{N+1}^2 + y_{N+1}y_1 + y_1^2)\Big)^2 + o(\epsilon^2) \qquad \text{(C5)} \end{aligned}$$

Let $A = (N-1)\ell_a$ be the total aperture of the array. Without loss of generosity, let $y_N = A/2$ and $y_1 = -A/2$. We separate (C5) into terms of different powers of ϵ:

$$O(\epsilon^0) \;=\; \frac{N^2\epsilon^0}{2\pi z_0}\sum_{l=1}^{B}|\omega_l| \tag{C6}$$

$$O(\epsilon) = \frac{iN^2\epsilon}{2\pi z_0^2}(y_N + y_1 - 2x_0)\sum_{l=1}^{B}|\omega_l|\omega_l = 0 \tag{C7}$$

$$\begin{aligned} O(\epsilon^2) \;&=\; \frac{N^2\epsilon^2}{2\pi z_0}\sum_{l=1}^{B}|\omega_l|\Big\{ -i\frac{\omega_l}{z_0} + \frac{\omega_l^2}{z_0^2}\Big(-2x_0^{\perp 2} + 2x_0(y_{N+1}+y_1) \\ &\quad -\frac{1}{3}(y_{N+1}^2 + y_{N+1}y_1 + y_1^2) - \frac{1}{4}(y_{N+1}+y_1)^2 - \frac{5}{12}\ell_a^2 + \ell_a(y_N + y_1 - 2x_0)\Big)\Big\} \\ &=\; \frac{N^2\epsilon^2}{2\pi z_0^3}\Big\{ -2x_0^2 - \ell_a^2 - \frac{A}{12}(A+2\ell_a)\Big\}\sum_{l=1}^{B}|\omega_l|^3 < 0 \end{aligned} \tag{C8}$$

The conditions (C7) and (C8) ensure that the point-target location is the local maximum of the imaging field (C3) along the cross-range direction. We define the (cross-range) resolution to be the (transverse) distance to the target location where u has dropped to half of its local maximum value and compute

$$\frac{O(\epsilon^2)}{O(\epsilon^0)} = \frac{\sum_{l=1}^{B}|\omega_l|^3}{2z_0^2\sum_{l=1}^{B}|\omega_l|}\Big\{ -2x_0^2 - \ell_a^2 - \frac{A}{12}(A+2\ell_a)\Big\}\epsilon^2 \tag{C9}$$

The resolution is inversely proportional to the square-root of the minus coefficient of ϵ^2. For $x_0 = 0$, $\ell_a \ll A$ and a narrow bandwidth $\omega_l \approx \omega$ we recover the classical Rayleigh formula $\sim z_0/(A\omega)$.

The other consequence of defining resolution as fixed percentage drop from the peak value of the imaging function is that for a fixed A the resolution decreases as ℓ_a increases (N decreases), resulting the optimal resolution with $N = 2$.

2. SA imaging

SA corresponds to having only the diagonal elements of the response matrices. In this case,

$$u(x,z) \;=\; \frac{1}{2\pi}\sum_{l=1}^{B}\sum_{n=1}^{N}|\omega_l|z_0^{-1}e^{2i\omega_l(z_0-z)}e^{-i\frac{\omega_l|x-y_n|^2}{z}}e^{i\frac{\omega_l|x_0-y_n|^2}{z_0}}.$$

Following the same calculation as above, we have

$$
\begin{aligned}
&u(z_0,x)\\
&= \frac{1}{2\pi z_0}\sum_{l=1}^{B}|\omega_l|\Big(e^{2i\ell_a\omega_l(x-x_0)/z_0}-1\Big)^{-1}e^{-i\frac{\omega_l}{z_0}(|x|^2-|x_0|^2)}\Big(e^{2i\frac{\omega_l}{z_0}(x-x_0)\cdot y_{N+1}}-e^{2i\frac{\omega_l}{z_0}(x-x_0)\cdot y_1}\Big)\\
&= \frac{N}{2\pi z_0}\sum_{l=1}^{B}|\omega_l|\Big(1-\frac{i\omega_l\ell_a\epsilon}{z_0}-\frac{\omega_l^2\ell_a^2\epsilon^2}{3z_0^2}\Big)\Big(1-i\epsilon\frac{2\omega_l x_0}{z_0}-\epsilon^2(i\frac{\omega_l}{z_0}+\frac{2\omega_l^2x_0^{\perp 2}}{z_0^2})\Big)\\
&\quad\times\Big(1+\frac{i\omega_l}{z_0}\epsilon(y_{N+1}+y_1)-\frac{2\omega_l^2}{3z_0^2}\epsilon^2(y_{N+1}^2+y_{N+1}y_1+y_1^2)\Big)+o(\epsilon^2).
\end{aligned}
$$

The break-down of terms of different powers of ϵ are:

$$
O(\epsilon^0) \;=\; \frac{N\epsilon^0}{2\pi z_0}\sum_{l=1}^{B}|\omega_l|
$$

$$
O(\epsilon^1) \;=\; \frac{iN\epsilon^1}{2\pi z_0^2}(y_N+y_1-2x_0)\sum_{l=1}^{B}|\omega_l|\omega_l=0 \tag{C10}
$$

$$
\begin{aligned}
O(\epsilon^2) \;&=\; \frac{N\epsilon^2}{2\pi z_0}\sum_{l=1}^{B}|\omega_l|\Big\{-i\frac{\omega_l}{z_0}+\frac{\omega_l^2}{z_0^2}\Big(-2x_0^{\perp 2}+2x_0(y_{N+1}+y_1)\\
&\quad-\frac{2}{3}(y_{N+1}^2+y_{N+1}y_1+y_1^2)-\frac{1}{3}\ell_a^2-2\ell_a x_0\Big)\Big\}\\
&=\; \frac{N\epsilon^2}{2\pi z_0^3}\Big\{-2x_0^2-\ell_a^2-\frac{A}{6}(A+2\ell_a)\Big\}\sum_{l=1}^{B}|\omega_l|^3<0
\end{aligned} \tag{C11}
$$

Again, the conditions (C10) and (C11) ensure that the point-target location is the local maximum of the imaging field (C10). The resolution is inversely proportional to the square-root of the following expression

$$
-\frac{O(\epsilon^2)}{\epsilon^2O(\epsilon^0)}=\frac{\sum_{l=1}^{B}|\omega_l|^3}{2z_0^2\sum_{l=1}^{B}|\omega_l|}\Big\{2x_0^2+\ell_a^2+\frac{A}{6}(A+2\ell_a)\Big\} \tag{C12}
$$

For $x_0=0$ and $\ell_a\ll A$, the above calculations predict a smaller resolution in the case of SA by a factor of $1/\sqrt{2}$ in view of (C9)-(C12).

Appendix D: Range Resolution

1. Imaging with the full response matrices

Setting $z = z_0$ we have

$$u(x, z_0) \;=\; \frac{1}{2\pi} \sum_{l=1}^{B} \sum_{n,j=1}^{N} |\omega_l| z_0^{-1} e^{-2i\omega_l \epsilon} e^{i\frac{\omega_l |x_0 - y_n|^2}{2}(-\frac{1}{z} + \frac{1}{z_0})} e^{i\frac{\omega_l |x_0 - y_j|^2}{2}(-\frac{1}{z} + \frac{1}{z_0})}$$

which can be approximated by

$$\frac{1}{2\pi \ell_a^2} \sum_{l=1}^{B} |\omega_l| z_0^{-1} e^{-2i\omega_l \epsilon} \Big(\int_{x_0 - (A+\ell_a)/2}^{x_0 + (A+\ell_a)/2} e^{i\frac{\omega_l |x_0 - y_n|^2}{2}(-\frac{1}{z} + \frac{1}{z_0})} dy_n \Big)^2$$

provided that the antennas are so finely spaced that the summation over y_n, y_j can be replaced by integral.

Calculating with up to the second-order-in-ϵ as before we have

$$\begin{aligned} \int_{-(A+\ell_a)/2}^{(A+\ell_a)/2} e^{ix^2 \Upsilon} dx \;&=\; \int_{-(A+\ell_a)/2}^{(A+\ell_a)/2} \Big(1 + ix^2 \Upsilon - \frac{1}{2} x^4 \Upsilon^2 + o(\Upsilon^2) \Big) dx \\ &=\; (A + \ell_a) + \frac{1}{12} i (A + \ell_a)^3 \Upsilon - \frac{1}{160} (A + \ell_a)^5 \Upsilon^2 + o(\Upsilon^2) \qquad \text{(D1)} \end{aligned}$$

and consequently

$$\begin{aligned} u(x, z_0) \;&=\; \frac{1}{2\pi \ell_a^2} \sum_{l=1}^{B} |\omega_l| z_0^{-1} e^{-2i\omega_l \epsilon} (A + \ell_a)^2 \\ &\quad \times \Big(1 + \frac{i(A + \ell_a)^2}{12} \frac{\omega_l \epsilon}{2 z_0 (z_0 + \epsilon)} - \frac{(A + \ell_a)^4}{160} \frac{\omega_l^2 \epsilon^2}{4 z_0^2 (z_0 + \epsilon)^2} + o(\epsilon^2) \Big)^2 \\ &=\; \frac{N^2}{2\pi} \sum_{l=1}^{B} |\omega_l| z_0^{-1} (1 - 2i\omega_l \epsilon - 2\omega_l^2 \epsilon^2 + o(\epsilon^2)) \Big\{ 1 + \frac{i(A + \ell_a)^2 \omega_l \epsilon}{12 z_0^2} \\ &\quad - \frac{(A + \ell_a)^4 \omega_l^2 \epsilon^2}{576 z_0^4} - \frac{i(A + \ell_a)^2 \omega_l \epsilon^2}{12 z_0^3} - \frac{(A + \ell_a)^4 \omega_l^2 \epsilon^2}{320 z_0^4} + o(\epsilon^2) \Big\}. \end{aligned}$$

The zero-th, first, and second order terms of ϵ are

$$O(\epsilon^0) = \frac{N^2\epsilon^0}{2\pi z_0}\sum_{l=1}^{B}|\omega_l| \tag{D2}$$

$$O(\epsilon^1) = \frac{iN^2\epsilon^1}{2\pi z_0}(-2+\frac{(A+\ell_a)^2}{12z_0^2})\sum_{l=1}^{B}|\omega_l|\omega_l = 0 \tag{D3}$$

$$\begin{aligned} O(\epsilon^2) &= \frac{N^2\epsilon^2}{2\pi}\sum_{l=1}^{B}|\omega_l|z_0^{-1}\Big\{-2\omega_l^2-\frac{i(A+\ell_a)^2\omega_l}{12z_0^3} \\ &\quad +\frac{(A+\ell_a)^2\omega_l^2}{6z_0^2}-\frac{7(A+\ell_a)^4\omega_l^2}{1440z_0^4}\Big\} \\ &= -\frac{N^2\epsilon^2}{2\pi z_0}\Big\{2-\frac{(A+\ell_a)^2}{6z_0^2}+\frac{7(A+\ell_a)^4}{1440z_0^4}\Big\}\sum_{l=1}^{B}|\omega_l|^3 < 0 \end{aligned} \tag{D4}$$

(D4) is negative since the propagation distance z_0 is typically larger than the aperture size A in the paraxial regime. The conditions (D3) and (D4) ensure that the point-target location is the local maximum of the mean imaging field (C10) in the longitudinal direction. The resolution is inversely proportional to the square-root of the following expression

$$-\frac{O(\epsilon^2)}{\epsilon^2 O(\epsilon^0)} = \frac{\sum_{l=1}^{B}|\omega_l|^3}{2\sum_{l=1}^{B}|\omega_l|}\Big\{2-\frac{(A+\ell_a)^2}{6z_0^2}+\frac{7(A+\ell_a)^4}{1440z_0^4}\Big\}. \tag{D5}$$

If we completely neglect the second and the third terms in (D5) then we obtain the longitudinal resolution

$$\sim\left(\frac{\sum_{l=1}^{B}|\omega_l|}{\sum_{l=1}^{B}|\omega_l|^3}\right)^{1/2}$$

which is inversely proportional to the bandwidth, a classical result. When we take into account the perturbative effect of the aperture, the change of sign in the second term in (D5) says that the resolution increases with A as manifest in the bottom plot of Figure 7. Also, contrary to the case of cross-range resolution, the range resolution increases, for a fixed A, as ℓ_a increases (N decreases).

2. SA imaging

Following the same calculation with the SA imaging function we have up to the second order in ϵ

$$\begin{aligned}
\mathbb{E}u(x_0,z) &= \frac{1}{2\pi}\sum_{l=1}^{B}\sum_{n=1}^{N}|\omega_l|z_0^{-1}e^{-2i\omega_l\epsilon}e^{-i\omega_l|x_0-y_n|^2(\frac{1}{z}-\frac{1}{z_0})} \\
&\approx \frac{1}{2\pi\ell_a}\sum_{l=1}^{B}|\omega_l|z_0^{-1}e^{-2i\omega_l\epsilon}\int_{x_0-(A+\ell_a)/2}^{x_0+(A\ell_a)/2}e^{-i\omega_l|x_0-y_n|^2(\frac{1}{z}-\frac{1}{z_0})}dy_n \\
&= \frac{1}{2\pi\ell_a}\sum_{l=1}^{B}\omega_l z_0^{-1}e^{-2i\omega_l\epsilon}(A+\ell_a) \\
&\quad\times\Big(1+\frac{i(A+\ell_a)^2}{12}\frac{\omega_l\epsilon}{z_0(z_0+\epsilon)}-\frac{(A+\ell_a)^4}{160}\frac{\omega_l^2\epsilon^2}{z_0^2(z_0+\epsilon)^2}+o(\epsilon^2)\Big) \\
&= \frac{N}{2\pi}\sum_{l=1}^{B}|\omega_l|z_0^{-1}(1-2i\omega_l\epsilon-2\omega_l^2\epsilon^2+o(\epsilon^2)) \\
&\quad\times\Big(1+\frac{i\omega_l(A+\ell_a)^2}{12z_0^2}\epsilon-\frac{i\omega_l(A+\ell_a)^2}{12z_0^3}\epsilon^2-\frac{\omega_l^2(A+\ell_a)^4}{160z_0^4}\epsilon^2+o(\epsilon^2)\Big)
\end{aligned}$$

Then the ϵ terms are given below,

$$O(\epsilon^0) = \frac{N\epsilon^0}{2\pi z_0}\sum_{l=1}^{B}|\omega_l| \tag{D6}$$

$$O(\epsilon^1) = \frac{iN\epsilon^1}{2\pi z_0}(-2+\frac{(A+\ell_a)^2}{12z_0^2})\sum_{l=1}^{B}|\omega_l|\omega_l = 0 \tag{D7}$$

$$O(\epsilon^2) = -\frac{N\epsilon^2}{2\pi z_0}\Big(2-\frac{(A+\ell_a)^2}{6z_0^2}+\frac{(A+\ell_a)^4}{160z_0^4}\Big)\sum_{l=1}^{B}|\omega_l|^3 < 0 \tag{D8}$$

The conditions (D7) and (D8) ensure that the point-target location is the local maximum of the imaging field (C10) along the range direction in the paraxial regime. The resolution is inversely proportional to the square-root of the following quantity

$$-\frac{O(\epsilon^2)}{\epsilon^2 O(\epsilon^0)} = \frac{\sum_{l=1}^{B}|\omega_l|^3}{2\sum_{l=1}^{B}|\omega_l|}\Big\{2-\frac{(A+\ell_a)^2}{6z_0^2}+\frac{(A+\ell_a)^4}{160z_0^4}\Big\}. \tag{D9}$$

Comparing (D9) with (D5) we see that the difference is in the third terms of the respective expressions resulting a slightly better resolution for the SA imaging.

---

[1] M. Cheney M, *A mathematical tutorial on synthetic aperture radar*, *SIAM Review*, (2001), 43, 301-312.

[2] M.L. Dennison and A.J. Devaney, *Inverse scattering in inhomogeneous background media: II. Multi-frequency case and SVD formulation. Inverse Problem* 20 (2004), 1307-1324.

[3] G.D. Durgin, *Space-Time Wireless Channels*, Prentice-Hall, New Jercey, 2003.

[4] A. Fannjiang, *Time reversal communication in Rayleigh fading broadcast channels with pinholes*, *Phys. Lett. A* 353/5 (2006), 389-397.

[5] A. Fannjiang, *Information transfer in disordered media by broadband time reversal: stability, resolution and capacity*, *Nonlinearity* 19 (2006) 2425-2439.

[6] A. C. Fannjiang and and K. Solna, *Broadband Resolution Analysis for Imaging with Measurement Noise*, *Journal of the Optical Society of America A*, 24, 6, (2007), 1623-1632.

[7] A. Fannjiang and K. Solna, *Time Reversal of Parabolic Waves and Two-Frequency Wigner Distribution*, *Discrete and Continuous Dynamical Systems*, 6, 4, (2006), 783-802.

[8] A. Fannjiang and P. Yan, *Multi-frequency imaging of multiple targets in Rician fading channels: stability and resolution. Inverse Problems* 23 (2007), 1801-1819.

[9] L.L. Foldy, The multiple scattering of waves, *Phys. Rev.* 67, 107-119, 1945.

[10] A. Ishimaru, *Wave Propagation and Scattering in Random Media.* Vol. 1, Academic Press, New York, 1978.

[11] A. Ishimaru, *Wave Propagation and Scattering in Random Media.* Vol. 2, Academic Press, New York, 1978.

[12] R.G. Newton, *Scattering Theory of Waves and Particles*, Second edition, Dover, New York, 1982.

[13] M. Lax, Multiple scattering of waves, *Rev. Modern. Phys.* **23**, 287-310, 1951.

[14] M. Lax, Multiple scattering of waves II, The effective field in dense systems*Phys, Rev.* **85**, 261-269, 1952.

[15] J.G. Proakis, *Digital Communications*, 4-th edition, McGraw-Hill, New York, 2001.

[16] H.C. Van der Hulst, *Light Scattering by Small Particles*, Dover, New York, 1981.

[17] J.W. Strohbehn, *Laser Beam Propagation in the Atmosphere*, Springer-Verlag, Berlin, 1978.

[18] B. Yazici, M. Cheney and C.E. Yarman, *Synthetic-aperture inversion in the presence of noise and clutter*, Inverse Problems 22, (2006), 1705-1729.